USGS
science for a changing world

Iron Mineralogy and Bioaccessibility of Dust Generated From Soils as Determined by Reflectance Spectroscopy and Magnetic and Chemical Properties—Nellis Dunes Recreational Area, Nevada

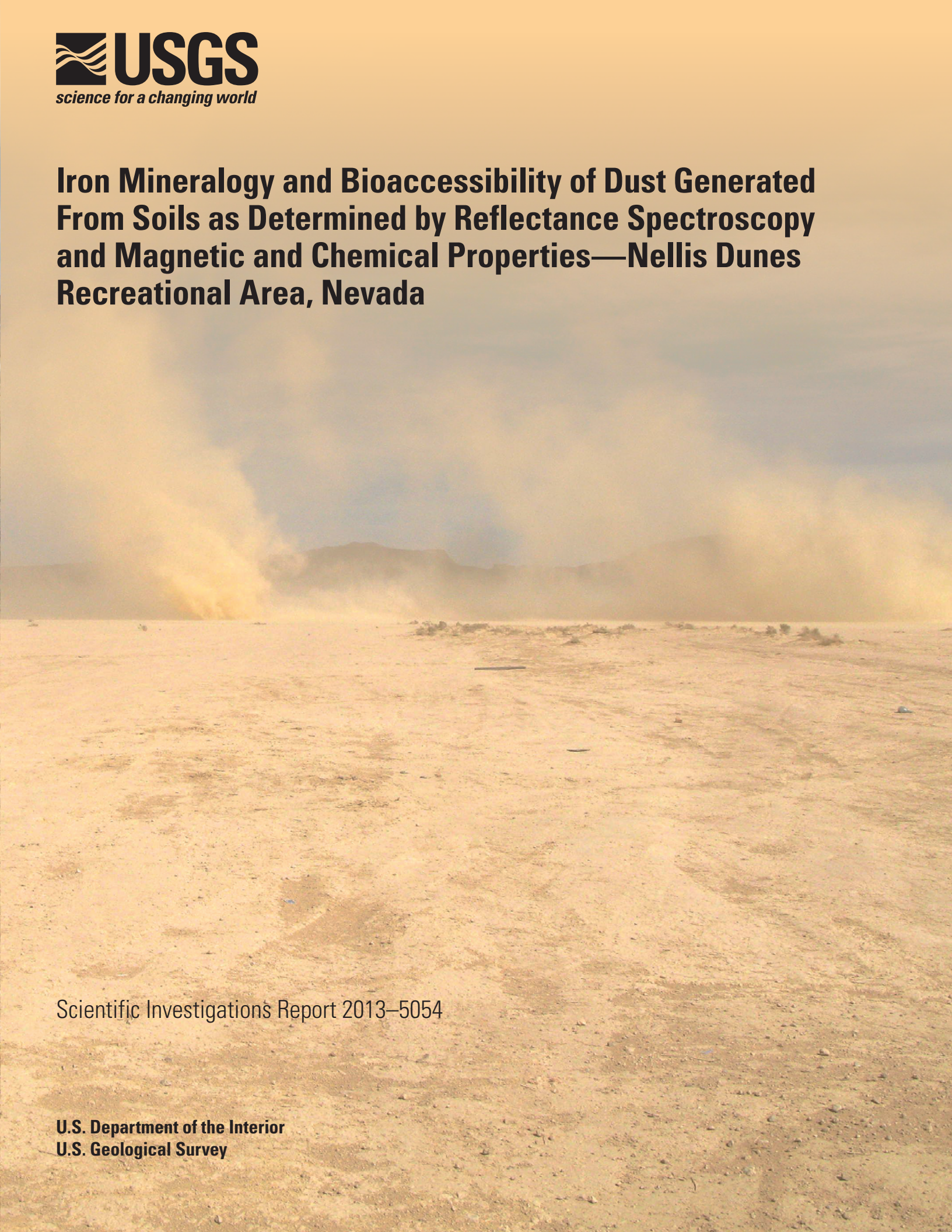

Scientific Investigations Report 2013–5054

U.S. Department of the Interior
U.S. Geological Survey

Front cover. Windy conditions produce dust emission from a silty surface at Nellis Dunes recreational area. Photo by Dirk Goossens.

Back cover. Photograph showing off-road-vehicle tracks at various landscape positions in the western portion of the Nellis Dunes recreational area. Photo by Dirk Goossens.

Iron Mineralogy and Bioaccessibility of Dust Generated From Soils as Determined by Reflectance Spectroscopy and Magnetic and Chemical Properties—Nellis Dunes Recreational Area, Nevada

By Harland L. Goldstein, Richard L. Reynolds, Suzette A. Morman, Bruce Moskowitz, Raymond F. Kokaly, Dirk Goossens, Brenda J. Buck, Cody Flagg, Jessica Till, Kimberly Yauk, and Thelma S. Berquó

Scientific Investigations Report 2013–5054

U.S. Department of the Interior
U.S. Geological Survey

U.S. Department of the Interior
KEN SALAZAR, Secretary

U.S. Geological Survey
Suzette M. Kimball, Acting Director

U.S. Geological Survey, Reston, Virginia: 2013

Suggested citation:
Goldstein, H.L., Reynolds, R.L., Morman, S.A., Moskowitz, Bruce, Kokaly, R.F., Goossens, Dirk, Buck, B.J., Flagg, Cody, Till, Jessica, Yauk, Kimberly, and Berquó, T.S., 2013, Iron mineralogy and bioaccessibility of dust generated from soils as determined by reflectance spectroscopy and magnetic and chemical properties—Nellis Dunes recreational area, Nevada: U.S. Geological Survey Scientific Investigations Report 2013–5054, 15 p., http://pubs.usgs.gov/sir/2013/5054/.

Contents

Figures

Tables

Conversion Factors and Datum

SI to Inch/Pound

Multiply	By	To obtain
	Length	
millimeter (mm)	0.03937	inch (in.)
meter (m)	3.281	foot (ft)
kilometer (km)	0.6214	mile (mi)
	Area	
square kilometer (km^2)	0.3861	square mile (mi^2)
	Flow rate	
meter per second (m/s)	3.281	foot per second (ft/s)
	Mass	
gram (g)	0.03527	ounce, avoirdupois (oz)
kilogram (kg)	2.205	pound avoirdupois (lb)

Temperature in degrees Celsius (°C) may be converted to degrees Fahrenheit (°F) as follows:

°F=(1.8×°C)+32.

Temperature in degrees Fahrenheit (°F) may be converted to degrees Celsius (°C) as follows:

°C=(°F-32)/1.8.

273.15 kelvin (K) is equal to 0.01 °C or 32.018 °F.

Abbreviations

χ_{hf}	high-field susceptibility
σ_{hys}	hysteresis shape
ARM	anhysteretic remanent magnetization
Av	vesicular A horizon
B_c	coercivity
B_{cr}	coercivity of remanence
B_{HF}	magnetic hyperfine field
DC	direct current
FC	field cooling
FDMS	frequency-dependent magnetic susceptibility
HIRM	hard isothermal remanent magnetization
ICP–MS	inductively coupled plasma–mass spectrometry
IRM	isothermal remanent magnetization
IS	isomer shift
IVBA	in vitro bioaccessibility analysis
LTIRM	low-temperature isothermal remanent magnetization
MICA	material identification and characterization algorithm
M_r	saturation remanence
MS	magnetic susceptibility
M_s	saturation magnetization
MS_{hf}	magnetic susceptibility high frequency
MS_{lf}	magnetic susceptibility low frequency
NDRA	Nellis Dunes recreational area
ORV	off-road vehicle
PRISM	Processing Routines in IDL for Spectroscopic Measurements (software)
QS	quadrupole splitting
R_{LT}	ratio between a low temperature SIRM imparted in a FC and a ZFC
RTSIRM	room-temperature saturation isothermal remanent magnetization
SGF	simulated gastric fluid
SIRM	saturation isothermal remanent magnetization
SLF	simulated lung fluid
SLyF	simulated phagolysosomal fluid
SOFIPEX	soil fine particle extractor technique
USGS	U.S. Geological Survey
ZFC	zero-field cooling

Acknowledgments

The Bureau of Land Management provided funding and granted permission to Dirk Goossens of the University of Nevada Las Vegas and the University of Leuven and Brenda J. Buck of the University of Nevada Las Vegas to conduct the original study for which these samples were collected. The analytical work was supported by the U.S. Geological Survey Climate and Land Use Change Program. Jiang Xiao of ADC Management Services provided laboratory assistance with reflectance spectroscopy and magnetic measurements. Jeremy Havens of ADC Management Services provided graphic assistance.

The Institute for Rock Magnetism is supported by grants from the Instruments and Facilities Program of the National Science Foundation Division of Earth Science.

We thank Gary Skipp and Frank Urban for their review of this report and helpful suggestions for improvement.

Iron Mineralogy and Bioaccessibility of Dust Generated From Soils as Determined by Reflectance Spectroscopy and Magnetic and Chemical Properties—Nellis Dunes Recreational Area, Nevada

By Harland L. Goldstein,[1] Richard L. Reynolds,[1] Suzette A. Morman,[1] Bruce Moskowitz,[2] Raymond F. Kokaly,[1] Dirk Goossens,[3,4] Brenda J. Buck,[3] Cody Flagg,[1] Jessica Till,[2] Kimberly Yauk,[2] and Thelma S. Berquó[5]

Abstract

Atmospheric mineral dust exerts many important effects on the Earth system, such as atmospheric temperatures, marine productivity, and melting of snow and ice. Mineral dust also can have detrimental effects on human health through respiration of very small particles and the leaching of metals in various organs. These effects can be better understood through characterization of the physical and chemical properties of dust, including certain iron oxide minerals, for their extraordinary radiative properties and possible effects on lung inflammation. Studies of dust from the Nellis Dunes recreation area near Las Vegas, Nevada, focus on characteristics of radiative properties (capacity of dust to absorb solar radiation), iron oxide mineral type and size, chemistry, and bioaccessibility of metals in fluids that simulate human gastric, lung, and phagolysosomal fluids. In samples of dust from the Nellis Dunes recreation area with median grain sizes of 2.4, 3.1, and 4.3 micrometers, the ferric oxide minerals goethite and hematite, at least some of it nanosized, were identified. In one sample, in vitro bioaccessibility experiments revealed high bioaccessibility of arsenic in all three biofluids and higher leachate concentration and bioaccessibility for copper, uranium, and vanadium in the simulated lung fluid than in the phagolysosomal fluid. The combination of methods used here to characterize mineral dust at the Nellis Dunes recreation area can be applied to global dust and broad issues of public health.

Introduction

Atmospheric dust can affect atmospheric temperatures, melting of snow and ice, marine productivity, and human health. Among mineral particles in dust, ferric oxide minerals possess important radiative properties, can stimulate phytoplankton productivity, and may contribute to inflammation in the human lung, but these minerals remain poorly described with respect to presence in far-traveled aerosol, specific mineralogy (hematite or goethite), particle size, and surface area (Formenti and others, 2010). The diverse effects of atmospheric dust can be better comprehended by characterization of iron minerals in dust. The distinction between hematite and goethite is useful for modeling the effects of dust on radiative forcing (that is, how dust affects the energy balance between incoming and outgoing solar radiation) in the atmosphere and in mountain snow and ice.

Results from studies of dust emission in the Nellis Dunes recreation area (NDRA; fig. 1) northeast of Las Vegas, Nevada, have been recently published by Goossens and Buck (2009a,b, 2011a,b) and Goossens and others (2012). This 37-square-kilometer (km^2) area is the most popular site in southern Nevada for off-road vehicle (ORV) driving. In addition to natural dust emissions caused by wind erosion, large amounts of dust are produced by ORV activity. The situation has attracted concern with respect to human health and air quality because of the proximity of the NDRA to Las Vegas (the NDRA is about 6 kilometers (km) from the northeastern margin of the city) and because the regional wind regime sends NDRA-emitted dust into the city during most of the winter.

[1]U.S. Geological Survey.

[2]University of Minnesota.

[3]University of Nevada Las Vegas.

[4]University of Leuven.

[5]Concordia College.

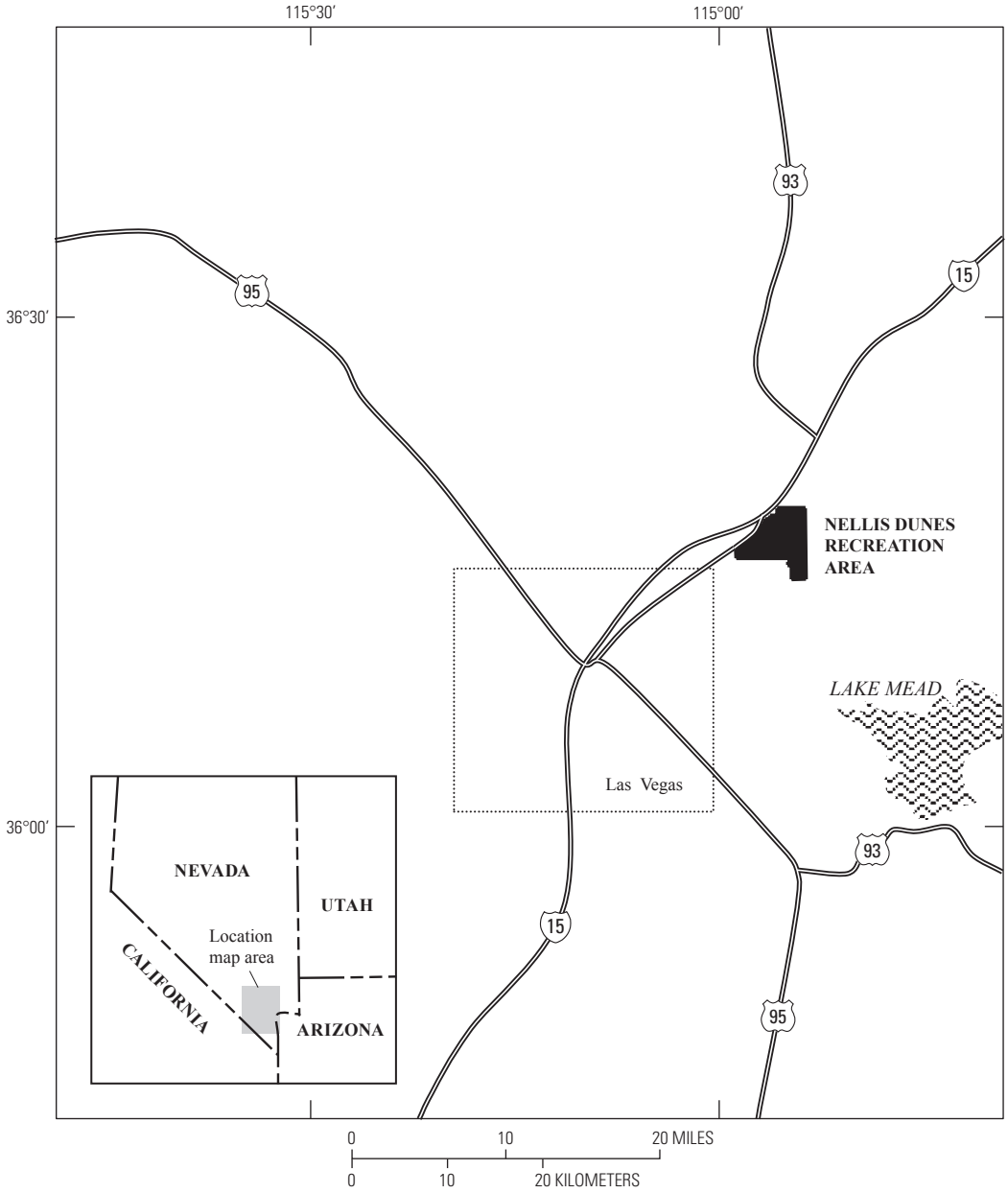

Figure 1. Map showing location of the Nellis Dunes recreation area in Nevada; modified from Goossens and Buck (2009a).

Four major types of surfaces occur in the NDRA: sand and sand-affected areas, silt and clay deposits, rock-covered sands and silts, and bedrock. Most ORV-produced dust from the NDRA is generated from the silt and clay and the rock-covered areas, the latter of which may contain a silty substratum—the vesicular A (Av) horizon—with a thin, discontinuous cover of rock fragments. Much less ORV-produced dust comes from the sand areas, and almost no dust comes from the bedrock areas (Goossens and Buck, 2011a,b).

Analytical results were obtained from three samples from the very uppermost soil for three units. The samples were obtained from bulk sediment dry fractionated to particle sizes 4.3 micrometers (μm) or less. According to the International Standards Organization's respirable convention curve, this size corresponds to a probability of 50 percent of penetration of respirable particles within workers' airways when working under a typical workload (Lee and others, 2011). Samples were collected from the following units:

- a silt and clay unit (described by McLaurin and others (2011b) as unit 2.2), rich in arsenic, with some surface gravel that forms a portion of badlands topography in the NDRA; median diameter after dry fractionation is 4.3 μm

- a well-developed desert pavement (described by McLaurin and others (2011b) as unit 3.1) with underlying silty Av soil horizon; median diameter after dry fractionation is 2.4 μm
- a rock-covered surface with silt and clay zones (described by McLaurin and others (2011b) as unit 3.2) that composes the greatest amount of surface area in the NDRA; median diameter after dry fractionation is 3.1 μm

All analyses were performed on less than a total of 2.5 grams of each dry fractionated sample. The purpose of our analyses was to characterize reflectance spectroscopy, magnetic, and chemical properties and bioaccessibility as a basis for better understanding (1) the relations between dust compositions and radiative properties and (2) potential health effects of dust emitted from the NDRA. The results presented here complement ongoing studies by others on NDRA dust (Goossens and Buck, 2011a,b; McLaurin and others, 2011a; Goossens and others, 2012; Soukup and others, 2012), and they add to the body of expanding information and data about the properties and effects of atmospheric dust (Reynolds and others, 2011).

Methods

Dry Fractionation and Particle Size Analysis

Samples were collected from the upper 2 to 3 centimeters (cm) of the topsoil, which produces the most dust when being disturbed by wind erosion or ORV driving. The samples were first dry sieved at 125 μm. The fraction that was less than 125 μm was then further dry fractionated to collect the fraction less than 4 μm using the soil fine particle extractor (SOFIPEX) technique described by Goossens (2012). This technique allows dry extraction of large volumes (dozens of grams and more) of fine particulate matter from bulk soil samples in a short time, usually in the order of minutes. After collection, the extracts were stored in plastic vials and then sent to the laboratory for further analysis.

Particle size distribution was determined with a Malvern Mastersizer S laser particle size analyzer. All analyses were done in water. No dispersion techniques were applied during the tests.

Reflectance Spectroscopy

Reflectance spectra of samples were measured to evaluate their mineral composition and to determine average reflectance values (table 1). Reflectance spectra were measured in the laboratory using an Analytical Spectral Devices, Inc., FieldSpec3 spectrometer, covering the wavelength range of 0.35 to 2.50 μm in 2,151 channels. A bidirectional reflectance measurement setup was used, with the light source and the fiber optic head of the spectrometer at fixed angles above the sample. For each sample, multiple reflectance measurements were made relative to a Labsphere, Inc., Spectralon white reference panel. The individual measurements were averaged, and the average spectrum (fig. 2) was converted to absolute reflectance using the U.S. Geological Survey (USGS) Processing Routines in IDL (interface description language software) for Spectral Measurements (PRISM; Kokaly, 2011) software.

Table 1. Spectral reflectance data.

[Sample ID, unique sample identification number. Total reflectance is average reflectance over entire wavelength range (0.35 to 2.50 micrometers (μm)). Visible reflectance is average reflectance over visible wavelengths (0.40 to 0.70 μm). Iron mineral fit, 1-μm minerals; dominant iron-bearing mineral identified. Fit values measure from 0 to 1 of the match of the identified mineral; highest values represent best match. Other mineral fit, 2-μm minerals; dominant other minerals identified. Other mineral fit results were derived from a different measurement than the iron mineral fit measurements due to potential influence from the background material in the 2- to 2.5-μm wavelength region. n.d.: not determined; —, none]

Sample ID	Total reflectance	Visible reflectance	Iron mineral fit	Iron mineral fit values	Other mineral fit	Other mineral fit values
Unit 2.2	0.620836	0.391134	—	n.d.	Montmorillonite_Ca	0.952
					Montmorillonite_Na	0.8541
Unit 3.1	0.646428	0.392579	Goethite	0.7591	Montmorillonite_Ca	0.9591
					Montmorillonite_Na	0.7941
					Muscovite_lowAl	0.7730
					Illite_gds4	0.7730
					Calcite.8+montmorillonite_Na.2	0.7503
Unit 3.2	0.584185	0.32341	Goethite	0.8031	Calcite.8+montmorillonite_Ca.2	0.9139
					Calcite.8+montmorillonite_Na.2	0.8174
					Muscovite_lowAl	0.8044
					Illite_gds4	0.7833
					Illite	0.6905

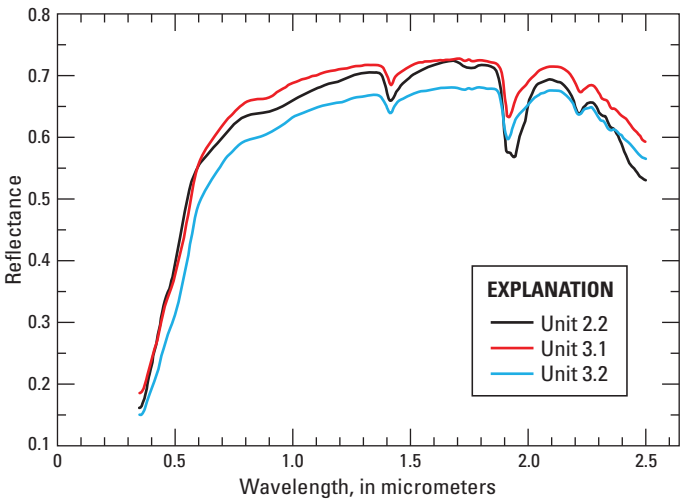

Figure 2. Chart showing absolute reflectance spectra obtained from averaged reflectance measurements made relative to Labsphere, Inc., Spectralon white reference panel for samples from the Nellis Dunes recreation area.

The mineral compositions of samples were characterized by analyzing their reflectance spectra with the material identification and characterization algorithm (MICA), a module of the PRISM software, which uses continuum removal to isolate diagnostic absorption features and linear regression to compare spectral features. MICA was used to compare the spectra of the Nellis Dunes samples to reference spectra of minerals and other materials in the USGS spectral library (version 6; Clark and others, 2007). Mineral spectra can be divided into two classes that are naturally separated in the wavelength regions of their primary absorption features: iron-bearing minerals with electronic absorption features centered primarily in the visible and near-infrared wavelengths (0.4 to 1.0 µm; commonly referred to as 1-µm minerals) and clays, carbonates, sulfates, and alteration-related minerals with vibrational absorption features centered primarily in the shortwave-infrared wavelengths (2.0 to 2.5 µm; commonly referred to as 2-µm minerals). The MICA analysis computes a fit value, ranging from 0 to 1, between the sample spectrum and each reference material (Kokaly, 2011). The reference spectrum with the highest fit value is termed the best fit.

Magnetic Properties

Magnetic properties provide information about the types, amounts, and grain sizes of magnetic iron oxide minerals. Magnetic properties at room temperature and at low temperatures (10–300 kelvin (K)) were determined on the dry-fractionated size fractions (table 2).

Table 2. Magnetic properties.—Continued

[Sample ID, unique sample identification number. HIRM is calculated as ($IRM_{1.2}$ + $IRM_{-0.3}$)/2. HIRM* is calculated as HIRM except that in place of a 1.2-T (tesla) field ($IRM_{1.2}$) a field of 1.0 T was used ($IRM_{1.0}$; data not shown). S ratio calculated as $IRM_{-0.3}$/$IRM_{1.2}$; n.d., not determined]

	Sample ID		
	Unit 2.2	Unit 3.1	Unit 3.2
Median grain size, in micrometers	4.3	2.4	3.1
Magnetic susceptibility, in cubic meters per kilogram:			
Low frequency	n.d.	3.87E-07	3.31E-07
High frequency	n.d.	3.74E-07	3.25E-07
Frequency-dependent magnetic susceptibility:			
Percent	n.d.	3.33	1.82
Cubic meters per kilogram	n.d.	1.29E-08	6.03E-09
Anhysteretic remanent magnetization, in ampere square meters per kilogram	n.d.	3.13E-04	2.88E-04
Isothermal remanent magnetization (IRM) from induction at room temperature, in ampere square meters per kilogram:			
In a 1.2-tesla (T) field, ($IRM_{1.2}$)	n.d.	5.84E-03	5.58E-03
In a 0.3-T field, ($IRM_{-0.3}$)	n.d.	4.99E-03	4.84E-03
Hard isothermal remanent magnetization, in ampere square meters per kilogram:			
For a 1.2-T field (HIRM)	n.d.	4.25E-04	3.71E-04
For a 1.0-T field (HIRM*)	5.48E-05	2.77E-04	2.52E-04
S ratio	n.d.	0.85	0.87
Saturation remanence (Mr), in ampere meter per kilogram	8.73E-04	5.81E-03	5.62E-03
Saturation magnetization (Ms), in ampere meter per kilogram	5.67E-03	3.28E-02	3.02E-02
Mr/Ms	0.15	0.18	0.19
Coercivity (Bc), in milliteslas	11.56	12.01	13.01

Table 2. Magnetic properties.—Continued

[Sample ID, unique sample identification number. HIRM is calculated as ($IRM_{1.2}$ + $IRM_{-0.3}$)/2. HIRM* is calculated as HIRM except that in place of a 1.2-T (tesla) field ($IRM_{1.2}$) a field of 1.0 T was used ($IRM_{1.0}$; data not shown). S ratio calculated as $IRM_{-0.3}/IRM_{1.2}$; n.d., not determined]

	Sample ID		
	Unit 2.2	**Unit 3.1**	**Unit 3.2**
Coercivity or remanence (Bcr), in milliteslas	35.54	34.91	37.00
Bcr/Bc	3.08	2.91	2.84
High field magnetic susceptibility, in cubic millimeters per kilogram	4.64E-08	7.08E-08	5.42E-08
Weight percent of magnetite	0.01	0.04	0.03
Hysteresis shape parameter (σ_{hys})	0.18	0.14	0.14

Magnetic Susceptibility

Magnetic susceptibility (MS) was measured by using a susceptometer with a sensitivity higher than about 2×10^{-9} cubic meters per kilogram. Samples were measured in a 0.1-millitesla (mT) induction at an MS low frequency (MS_{lf}) of 600 hertz (Hz) and MS high frequency (MS_{hf}) of 6,000 Hz. For each sample, the MS value was calculated as the mean of four measurements. Frequency-dependent magnetic susceptibility (FDMS) was calculated as follows:

$$\mathrm{FDMS} = \frac{\mathrm{MS_{lf}} - \mathrm{MS_{hf}}}{\mathrm{MS_{if}}} . \quad (1)$$

Laboratory-Induced Magnetization at Room Temperature

Measurements from anhysteretic remanent magnetization (ARM) and isothermal remanent magnetization (IRM) experiments were made by using a high-speed spinner magnetometer. Anhysteretic remanent magnetization was imparted in a decreasing alternating field from a peak induction of 100 mT and a direct current (DC) bias of 0.1 mT. IRM was generated at room temperature by using an impulse magnetizer. First, IRM was imparted in a 1.2-tesla (T) induction ($IRM_{1.2T}$). The samples then were magnetized in the opposite direction by using an induction of 0.3 T ($IRM_{-0.3T}$).

Hard isothermal remanent magnetization (HIRM; a measure of ferric oxide content) and the S-ratio (a measure of the relative amounts of low-coercivity phases (for example, magnetite and maghemite) to high-coercivity phases (for example, hematite and goethite)) were calculated as follows (King and Channel, 1991):

$$\mathrm{HIRM} = \frac{\mathrm{IRM_{1.2T}} + \mathrm{IRM_{-0.3T}}}{2} , \text{ and} \quad (2)$$

$$\mathrm{S} = \frac{\mathrm{IRM_{-0.3T}}}{\mathrm{IRM_{1.2T}}} . \quad (3)$$

S-ratio values near 1 indicate a high proportion of magnetite to hematite. Goethite is extremely hard to magnetize at room temperature in fields below 2.0 T (Rochette and others, 2005) and will contribute a negligible amount to HIRM or the S-ratio value even though it may be the abundant phase.

Hysteresis loops and backfield remanence curves at room temperature were measured on a vibrating-sample magnetometer using a saturating field of 1.0 T. Magnetic parameters determined from the hysteresis data include saturation magnetization (M_s), saturation remanence (M_r), coercivity (B_c), coercivity of remanence (B_{cr}), and high-field susceptibility (χ_{hf}). The shape of the loop was quantified using the hysteresis shape (σ_{hys}) parameter of Fabian (2003). Hysteresis shape parameters were determined after the loops were corrected for high-field slopes using the approach to saturation fitting described in Jackson and Solheid (2010). Coercivity of remanence was determined from DC backfield remanence curves. Samples were first given a remanence in a positive 1.0-T field and subsequently exposed to negative fields of increasing strength to 300 mT. The field where the remanence is zero is the coercivity of remanence. The magnetite weight percent was determined from the room-temperature bulk saturation magnetization values and the known value for pure magnetite (M_s=92 ampere square meters per kilogram (Am^2/kg)) as follows:

$$\text{Magnetite weight percent} = \frac{\mathrm{M_s}}{92 \ \frac{\mathrm{Am^2}}{\mathrm{kg}}} \times 100 \text{ percent} . \quad (4)$$

Laboratory-Induced Magnetization at Low Temperature

Low-temperature (10–300 K) magnetic properties were measured using a Quantum Design, Inc., Magnetic Properties Measurement System. Low-temperature isothermal remanent magnetization (LTIRM) was imparted using a 2.5-T field on samples that had been cooled to 10 K in the absence (zero-field cooling, ZFC) or presence (field cooling, FC) of a 2.5-T magnetic field. LTIRM was measured on warming in zero field to 300 K in 5-K increments. Samples were also given an IRM in a field of 2.5 T at 300 K (room-temperature saturation isothermal remanent magnetization; RTSIRM), and magnetization was measured during cooling to 10 K and during warming back to 300 K in zero field at 5-K increments. The low temperature remanence ratio (R_{LT}) was calculated to describe the shapes of the FC and ZFC curves (Liu and others, 2006; Smirnov, 2009), as follows:

$$R_{LT} = \frac{IRM(10K)_{FC}}{IRM(10K)_{ZFC}}, \quad (5)$$

where

$IRM(10K)_{FC}$ is field cooling IRM at 10 K and
$IRM(10K)_{ZFC}$ is zero-field cooling IRM at 10 K.

Mössbauer Spectroscopy

Mössbauer spectra were measured at 4.2 K and 300 K on dry-fractionated size fractions for two samples (from units 2.2 and 3.2) to characterize iron oxide mineralogy and to determine iron phases present. Measurements were made at 4.2 K using a conventional constant-acceleration spectrometer in transmission geometry with a cobalt-57 and rhodium (^{57}Co/Rh) source. An alpha-iron foil at room temperature was used to calibrate isomer shifts and velocity scale. The magnetic hyperfine parameters (table 3) including the hyperfine field (B_{HF}), isomer shift (IS), and quadrupole splitting (QS) were fit using the NORMOS program (Brand, 1987).

Chemical Properties

Total Chemical Composition

Dry-fractionated samples were analyzed to determine their chemical composition using inductively coupled plasma–mass spectrometry (ICP–MS) following acid digestion (Briggs and Meier, 2002). Chemical composition is represented by 37 major, minor, and trace elements (table 4).

Table 3. Mössbauer spectroscopy.

[Sample ID, unique sample identification number. K, kelvin; B_{HF}, magnetic hyperfine field, expressed in tesla (T). IS, isomer shift, expressed in millimeters per second (mm/s). QS, quadrupole splitting, expressed in mm/s. Iron phase, iron-bearing phases. %, percentage of total iron that the iron phases compose. —, not available]

Sample ID	4.2 K					300 K				
	B_{HF}	IS	QS	Iron phase	%	B_{HF}	IS	QS	Iron phase	%
Unit 2.2	49.8	0.50	–0.24	Goethite	32	—	—	—	Goethite	—
	—	0.50	0.54	Fe3+	63	—	0.38	0.58	Fe3+	90
	—	1.30	2.97	Fe3+	5	—	1.1	2.59	Fe2+	10
Unit 3.2	53.5	0.50	–0.03	Hematite	11	50.3	0.33	–0.16	Hematite	13
	49.1	0.50	–0.20	Goethite	26	—	—	—	Goethite	—
	—	1.18	3.05	Fe2+	8	—	1.00	2.86	Fe2+	14
	—	0.52	1.11	Fe3+	22	—	0.42	1.10	Fe3+	26
	—	0.50	0.43	Fe3+	33	—	0.37	0.45	Fe3+	47

Table 4. Geochemical data determined by inductively coupled plasma–mass spectrometry.

[Values are in parts per million. Sample ID, unique sample identification]

Sample ID	Unit 2.2	Unit 3.1	Unit 3.2
Aluminum	48,300	73,200	58,700
Antimony	0.743	1.02	1.08
Arsenic	145	22.7	23.4
Barium	921	521	465
Beryllium	1.38	1.78	1.62
Bismuth	0.422	0.463	0.394
Cadmium	0.263	0.39	0.619
Calcium	151,000	75,700	124,000
Cerium	54.2	71.7	62.7
Cesium	14.5	10.1	7.6
Chromium	34.6	56.1	60.7
Cobalt	6.79	11.8	9.75
Copper	75.9	41.2	48.4
Gallium	11.3	17.3	13.5
Iron	21,900	29,700	23,800
Lanthanum	34.1	38.8	35.2
Lead	19.7	21.6	18.4
Lithium	50.8	53.6	39.9
Magnesium	12,800	25,400	24,200
Manganese	259	570	498
Molybdenum	4.76	2.61	2.47
Nickel	7.61	24.5	19.1
Niobium	13	16.4	14.4
Phosphorus	525	1,070	786
Potassium	13,800	21,900	18,900
Rubidium	75.4	108	85.5
Scandium	7.44	11.3	9.35
Silver	0.085	0.098	0.071
Sodium	1,300	2,480	2,380
Strontium	549	245	404
Thallium	0.963	0.831	0.647
Thorium	9.33	13.5	11.2
Titanium	2,110	2,890	2,530
Uranium	6.16	3.03	3.37
Vanadium	94.1	80	73.4
Yttrium	24.9	26.5	25.4
Zinc	71.7	109	96.8

In Vitro Bioaccessibility Analysis

In vitro bioaccessibility analyses (IVBAs) are physiologically based extraction tests used to estimate the bioaccessibility of metals and metalloids along human exposure pathways. Bioaccessibility is defined as the amount of an element soluble in a simulated gastric fluid and available for uptake by the body (Ruby and others, 1996). Our IVBA tests simulated gastric, lung, and phagolysosomal fluids. The methodology of leaching Earth materials with fluids compositionally similar to those of the human body is used widely to examine the effects of contaminants on human health. All extraction solutions were analyzed by ICP–MS (table 5; Lamothe and others, 2002). Duplication of IVBA extractions was not possible due to the very small amount of sample available.

The simulated gastric fluid (SGF; with a pH of 1.5) extraction method (Morman and others, 2009) used here is based on a method developed by Drexler and Brattin (2007) and approved by the U.S. Environmental Protection Agency (2008) to measure bioaccessibility of lead. This method is currently being reviewed for use in determining arsenic bioaccessibility (Bradham and others, 2011). Simulated gastric fluid extraction samples are typically sieved to less than 250 µm because particulates of this size fraction or smaller are most likely to adhere to the hands of children and be ingested (Van Wijnen and others, 1990); however, our tests were performed on the dry-fractionated samples of much smaller particle sizes.

Application of IVBA tests to inhalation pathways is a relatively new technique, and these methods have not been accepted for regulatory purposes. Nevertheless, simulated lung (SLF) and phagolysosomal (SLyF) fluids (Herting and others, 2006; Stefaniak and others, 2005, 2006) permit modeling of in vivo solubility, an important physiochemical factor. The SLF has neutral pH (7.4), whereas the SLyF simulates the pH (4.5) that is present when particles are engulfed by pulmonary alveolar macrophages, which are the specialized lung cells involved in particle removal from the lung. Samples for SLF and SLyF extractions are usually sieved to less than 20 µm. This fraction is an approximation of the size deemed to be respirable (generally less than 5 µm). Our tests were performed on the dry-fractionated samples with median grain sizes comparable to respirable size fractions.

Table 5. Total bulk sample concentration and leachate concentration, percent bioaccessibility, and milligram leached per kilogram of solid for selected elements as measured in simulated gastric, lung, and phagolysosomal fluid.

[Sample ID, unique sample identification number. mg/kg, milligrams per kilogram; µg/L, micrograms per liter; n.d., no value could be calculated because leachate concentration was less than method detection limit; ppm, parts per million; <, value was less than the method reporting limit; *, calculated value resulted in a negative number because of blank correction; %, percent]

Sample ID	Total, in ppm	Leachate, in µg/L	% bioaccessible	Leached, in mg/kg of solid	Total, in ppm	Leachate, in µg/L	% bioaccessible	Leached, in mg/kg of solid
	Aluminum				**Arsenic**			
	Gastric				Gastric			
Unit 2.2	48,300	10,700	2.21	1,069	145	739	50.6	73.4
Unit 3.1	73,200	24,700	3.37	2,469	22.7	59.1	23.8	5.41
Unit 3.2	58,700	18,100	3.08	1,809	23.4	61.2	24.0	5.62
	Lung				Lung			
Unit 2.2	48,300	<20	n.d.	n.d.	145	119	7.86	11.4
Unit 3.1	73,200	24.6	*	*	22.7	<10	n.d.	n.d.
Unit 3.2	58,700	175	0.022	12.9	23.4	17.0	5.13	1.20
	Phagolysosomal				Phagolysosomal			
Unit 2.2	48,300	<20	n.d.	n.d.	145	285	19.7	28.5
Unit 3.1	73,200	<20	n.d.	n.d.	22.7	20.3	8.94	2.03
Unit 3.2	58,700	<20	n.d.	n.d.	23.4	23.6	10.1	2.36
	Barium				**Cadmium**			
	Gastric				Gastric			
Unit 2.2	921	650	7.01	64.6	0.263	2.34	86.2	0.224
Unit 3.1	521	2,560	49.1	256	0.390	3.43	85.4	0.333
Unit 3.2	465	2,420	52.0	242	0.619	6.49	103	0.639
	Lung				Lung			
Unit 2.2	921	29.4	0.319	2.94	0.260	<0.2	n.d.	n.d.
Unit 3.1	521	330	6.33	33.0	0.390	<0.2	n.d.	n.d.
Unit 3.2	465	79.6	1.71	7.96	0.620	<0.2	n.d.	n.d.
	Phagolysosomal				Phagolysosomal			
Unit 2.2	921	184	1.88	17.4	0.260	0.330	12.7	0.033
Unit 3.1	521	932	17.7	92.2	0.390	0.400	10.3	0.040
Unit 3.2	465	491	10.3	48.1	0.620	0.680	11.0	0.068
	Chromium				**Copper**			
	Gastric				Gastric			
Unit 2.2	34.6	102	*	*	75.9	436	57.1	43.4
Unit 3.1	56.1	122	1.16	1.00	41.2	62.4	14.5	5.99
Unit 3.2	60.7	148	5.35	3.25	48.4	188	38.3	18.6
	Lung				Lung			
Unit 2.2	34.6	<10	n.d.	n.d.	75.9	394	51.6	39.2
Unit 3.1	56.1	<10	n.d.	n.d.	41.2	55.4	12.8	5.29
Unit 3.2	60.7	14.8	1.61	0.980	48.4	180	36.7	17.8
	Phagolysosomal				Phagolysosomal			
Unit 2.2	34.6	<10	n.d.	n.d.	75.9	257	33.9	25.7
Unit 3.1	56.1	<10	n.d.	n.d.	41.2	29.4	7.14	2.94
Unit 3.2	60.7	10.1	*	*	48.4	99.2	20.5	9.92
	Iron				**Lead**			
	Gastric				Gastric			
Unit 2.2	21,900	892	0.293	64.2	19.7	105	52.6	10.4
Unit 3.1	29,700	1,240	0.333	99.0	21.6	74.1	33.7	7.28
Unit 3.2	23,800	1,380	0.475	113	18.4	77.8	41.6	7.65

Table 5. Total bulk sample concentration and leachate concentration, percent bioaccessibility, and milligram leached per kilogram of solid for selected elements as measured in simulated gastric, lung, and phagolysosomal fluid.—Continued

[Sample ID, unique sample identification number. mg/kg, milligrams per kilogram; µg/L, micrograms per liter; n.d., no value could be calculated because leachate concentration was less than method detection limit; ppm, parts per million; <, value was less than the method reporting limit; *, calculated value resulted in a negative number because of blank correction; %, percent]

Sample ID	Total, in ppm	Leachate, in µg/L	% bioaccessible	Leached, in mg/kg of solid	Total, in ppm	Leachate, in µg/L	% bioaccessible	Leached, in mg/kg of solid
	Iron				**Lead**			
	Lung				Lung			
Unit 2.2	21,900	<500	n.d.	n.d.	19.7	<0.5	n.d.	n.d.
Unit 3.1	29,700	<500	n.d.	n.d.	21.6	<0.5	n.d.	n.d.
Unit 3.2	23,800	<500	n.d.	n.d.	18.4	<0.5	n.d.	n.d.
	Phagolysosomal				Phagolysosomal			
Unit 2.2	21,900	<500	n.d.	n.d.	19.7	0.670	*	*
Unit 3.1	29,700	<500	n.d.	n.d.	21.6	<0.5	n.d.	n.d.
Unit 3.2	23,800	<500	n.d.	n.d.	18.4	<0.5	n.d.	n.d.
	Manganese				**Uranium**			
	Gastric				Gastric			
Unit 2.2	259	1,110	42.8	111	6.16	24.6	39.1	2.41
Unit 3.1	570	1,210	21.2	121	3.03	4.49	13.2	0.399
Unit 3.2	498	1,410	28.3	141	3.37	9.66	27.2	0.916
	Lung				Lung			
Unit 2.2	259	24.0	0.888	2.30	6.16	5.02	7.34	0.452
Unit 3.1	570	14.2	0.232	1.32	3.03	<1	n.d.	n.d.
Unit 3.2	498	13.2	0.245	1.22	3.37	2.53	6.02	0.203
	Phagolysosomal				Phagolysosomal			
Unit 2.2	259	201	0.008	20.1	6.16	1.97	0.003	0.197
Unit 3.1	570	86.9	0.002	8.69	3.03	<1	n.d.	n.d.
Unit 3.2	498	67.9	0.001	6.79	3.37	<1	n.d.	n.d.
	Vanadium				**Zinc**			
	Gastric				Gastric			
Unit 2.2	94.1	204	18.9	17.8	71.7	113	11.3	8.11
Unit 3.1	80.0	49.4	2.88	2.30	109	83.6	4.74	5.17
Unit 3.2	73.4	62.6	4.93	3.62	96.8	110	8.07	7.81
	Lung				Lung			
Unit 2.2	94.1	75.9	7.80	7.34	71.7	<5	n.d.	n.d.
Unit 3.1	80.0	11.7	1.15	0.920	109	<5	n.d.	n.d.
Unit 3.2	73.4	30.7	3.84	2.82	96.8	<5	n.d.	n.d.
	Phagolysosomal				Phagolysosomal			
Unit 2.2	94.1	52.8	0.006	5.28	71.7	<30	n.d.	n.d.
Unit 3.1	80.0	6.30	0.001	0.630	109	<30	n.d.	n.d.
Unit 3.2	73.4	14.3	0.002	1.43	96.8	<30	n.d.	n.d.

Results

Reflectance Spectroscopy

Average reflectance values range from 0.5842 to 0.6464 (table 1) across the entire wavelength range of the instrument (average total reflectance), and from 0.3234 to 0.3926 across the visible wavelength region, 0.40 to 0.70 µm (average visible reflectance). Diagnostic absorption features arising from the minerals in the samples were centered near 0.51 µm, 0.90 µm, and 2.21 µm. Generally, the absorption features in the sample spectra were weak, as determined by the shallow band depth of the absorption features (see the discussion of band depth in Kokaly, 2011). The weak absorption features near 2.3 µm may be caused, in part, by absorption by the plastic background behind the samples.

The absorption features in the 1-µm region of the spectra of the samples from units 3.1 and 3.2 were matched to the reference spectrum of a thin coating of goethite on quartz (table 1; Clark and others, 2007). The wavelength positions of these weak absorption features indicate that the goethite is in low abundance and fine-grained or possibly nanocrystalline. Absorption features in the sample from unit 2.2 were even weaker, and the spectrum was not matched to any of the reference spectra of iron-bearing minerals.

The absorption features in the 2-µm region indicate the presence of montmorillonite clay in low abundance in the sample from unit 2.2 (table 1); the sample's spectrum matched the calcium-rich montmorillonite reference spectrum with a higher fit value as opposed to the sodium-rich montmorillonite reference spectrum. Samples from units 3.1 and 3.2 are best matched by the reference spectrum of calcium-rich montmorillonite clay and a mixture of calcite (80 percent) and calcium-rich montmorillonite clay (20 percent), respectively (calcite.8+montmorillonite_Ca.2, table 1). Lower fits to other reference spectra indicate the possibility that trace amounts of illite and (or) muscovite may be present in the samples from units 3.1 and 3.2. Reference spectra of calcite have a 2.3-µm absorption feature. An absorption feature near this position is present in the sample from unit 3.1 but does not have a high fit to the reference feature. Therefore, the weak spectral feature in this sample indicates calcite is present in a lower abundance than the other minerals.

Magnetic Properties

Hysteresis and Low-Temperature Results

At high fields, the hysteresis loops show a positive-slope characteristic of paramagnetic or antiferromagnetic minerals. After correction for the high-field susceptibility (Jackson and Solheid, 2010), the hysteresis loops display magnetic behavior typical of ferrimagnetic minerals like magnetite. However, the σ_{hys} parameters were all greater than zero, indicating a slight wasp-waisted shape due to a possible mixture of low- and high-coercivity minerals (Fabian, 2003). Magnetite and titanomagnetite are common low-coercivity minerals, and ferric oxide minerals, such as hematite and goethite, are common high-coercivity minerals. The presence of magnetite was confirmed by the RTSIRM curves showing the characteristic Verwey transition (Verwey, 1939) of magnetite (Verwey transition temperature (T_V) is about 120 K) in all three samples (fig. 3), but the abundance of magnetite is extremely low. From the M_s values at room temperature, the weight percent of magnetite was found to vary from 60 parts per million (ppm; sample from unit 2.2) to 360 ppm (samples from units 3.1 and 3.2). The remanence (M_r/M_s) and coercivity (Bcr/Bc) ratios have values typical of pseudo-single-domain magnetite particles (magnetic grain sizes about 1–10 µm). HIRM values were larger in units 3.1 and 3.2 than in unit 2.2, indicating higher concentrations of high-coercivity minerals (like hematite) in units 3.1 and 3.2.

The FC and ZFC remanent magnetization curves show continuous decreases in magnetization with increasing temperature coupled with FC curves displaying stronger magnetizations than the corresponding ZFC curves until converging near 300 K (fig. 4). There was no indication of the Morin (1950) transition (temperature = 250–260 K) associated with coarse-grained, crystalline hematite in any of the three samples, but there was a minor expression of the Verwey transition associated with magnetite in samples 3.1 and 3.2. The R_{LT} ratio was 2.7 for sample 2.2 and 1.4 for samples 3.1 and 3.2. The FC–ZFC behavior represented by the R_{LT} ratio values confirms

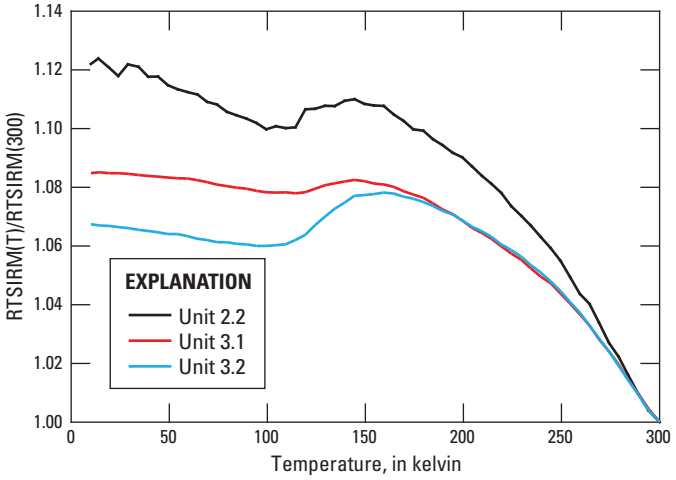

Figure 3. Chart showing temperature dependence of room-temperature saturation isothermal remanence magnetization (RTSIRM) in zero field on cooling (ZFC) to 10 kelvin (K) for samples from the Nellis Dunes recreation area. The magnetizations during ZFC (RTSIRM(T)) are normalized to the initial magnetization at 300 K (RTSIRM(300)), which was imparted at 300 K in a 2.5-tesla field. The drop in magnetization near 120 K is the Verwey transition in magnetite.

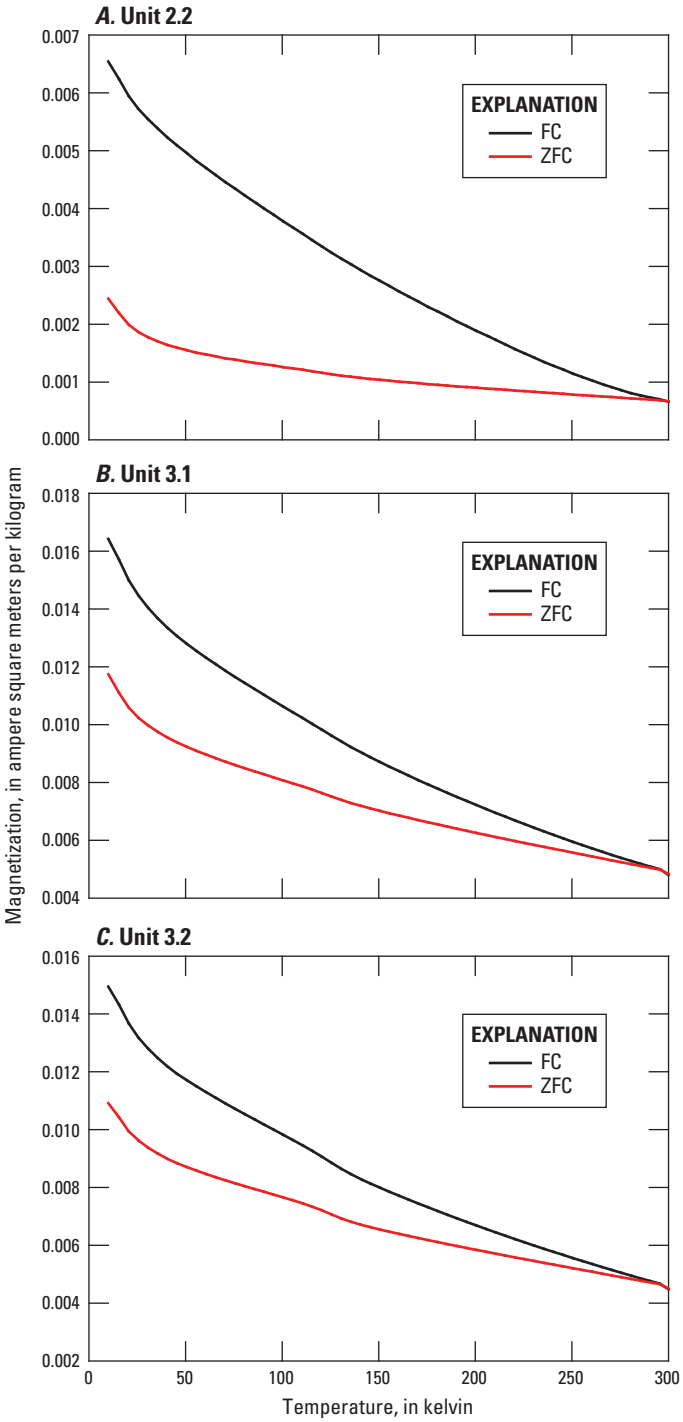

Figure 4. Charts showing thermal demagnetization of low-temperature isothermal remanent magnetization (LTIRM) imparted at 10 K after cooling in a zero field (ZFC) and in a 2.5-tesla magnetic field (FC) for samples from *A*, unit 2.2, *B*, unit 3.1, and *C*, unit 3.2 from the Nellis Dunes recreation area. The remanence is measured on warming to 300 K.

the presence of a mineral that has high coercivity and is not saturated in a 2.5-T field, which is consistent with a significant fraction of goethite in all three samples (Guyodo and others, 2003; Liu and others, 2006; Smirnov, 2009). Furthermore, the higher R_{LT} ratio in the sample from unit 2.2 compared with those in the samples from units 3.1 and 3.2 indicates that the sample from unit 2.2 has a larger fraction of goethite relative to magnetite. In pure end-member cases, magnetite has R_{LT} ratios less than 1.4 (Smirnov, 2009), but goethite can have R_{LT} ratios greater than 2.0 (Guyodo and others, 2003; Liu and others, 2006).

Mössbauer Spectroscopy

The Mössbauer spectra at 4.2 K and 300 K for the samples from units 2.2 and 3.2 were fit to multiple doublets and sextets representing magnetically ordered goethite and hematite, and paramagnetic ferric (Fe^{3+}) and ferrous (Fe^{2+}) phases. The hyperfine parameters are listed in table 3. At 4.2 K, the spectra are dominated by Fe^{3+} paramagnetic doublets (more than 50 percent of total iron). However, due to the broadened resonant peaks and multiple components, it was not possible at the time of the study to assign specific mineral phases to the paramagnetic doublets. Goethite was detected in both samples and composed approximately 30 percent of the iron-bearing phases. A smaller amount of hematite (11 to 13 percent) was also detected in the sample from unit 3.2 at 4.2 K and 300 K. It was not possible to obtain reliable fits for magnetite in either sample because it occurred in such low concentrations (less than 0.1 percent, as determined from magnetization experiments) that it was well below the detection limits (about 1 percent of total iron) for Mössbauer spectroscopy.

Mössbauer analysis for samples from units 2.2 and 3.2 was also carried out at 300 K. The characteristic sextet associated with goethite found at 4.2 K was missing at 300 K and reflects complete magnetic order for goethite only at very low temperatures even though the Néel temperature for pure goethite is about 373 K. The difference between the 4.2 K and 300 K spectra is due to magnetic relaxation and shows that goethite is superparamagnetic at 300 K and exhibits a doublet (unblocked and cannot carry remanence) but becomes blocked at temperatures higher than 300 K. This confirms that a significant fraction of goethite occurs as nanogeothite with particle sizes less than about 20 nanometers (nm). This size fraction will not contribute to remanence properties (saturation isothermal remanent magnetization (SIRM), HIRM) at 300 K.

A magnetically ordered sextet for hematite is observed at 4.2 K and 300 K in the sample from unit 3.2, indicating that most of the hematite is not superparamagnetic for temperatures less than or equal to 300 K and will contribute to room-temperature remanence properties (SIRM, HIRM). Moreover, the quadrupole splitting (QS) parameter at 4.2 K is negative (table 3), indicating that a significant fraction of the hematite phase in the sample from unit 3.2 is still above the Morin transition even at 4.2 K and is still in its canted antiferromagnetic

state. This is consistent with the absence of the characteristic Morin transition for hematite in the LTIRM remanence curves. Suppression of the Morin transition in hematite can occur due to reduced crystallinity, cation substitution (for example, titanium (IV) and aluminum (III)), or small particle effects (diameter (d) less than 100 nm; Murad and Johnston, 1987). The presence of hematite in unit 3.2 is also consistent with HIRM values.

In Vitro Bioaccessibility

Leaching results for selected elements vary in solubility relative to the pH of the IVBA fluids (table 5). In general, solubility and bioaccessibility of elements were lowest in the neutral pH SLF and highest in the SGF. The elevated bioaccessibility and total concentration of arsenic in all fluids in the sample from unit 2.2 indicate large concentrations of leached arsenic per kilogram of solid. Three metals (copper, uranium, and vanadium) have a higher leachate concentration and bioaccessibility in the SLF than in the SLyF. Despite total iron concentrations from nearly 22,000 to 29,000 ppm, iron bioaccessibility is minimal in the SGF (less than 0.5 percent), and leach concentrations were below the detection limit in the SLF and the SLyF.

Discussion

Iron oxide minerals, and especially the ferric oxides such as hematite and goethite, are important for issues of atmospheric dust. The iron oxide minerals in dust are capable of absorbing solar radiation. Whereas strongly magnetic (ferrimagnetic) magnetite (Fe_3O_4) depresses reflectance across the full spectrum of solar radiation, the weakly magnetic (antiferromagnetic) ferric oxide minerals have capacity to absorb strongly in the visible and near-infrared wavelengths. Radiative properties of iron oxide minerals thus have an effect on the ways by which dust can affect weather and climate (Gassó and others, 2010) and the melting of snow and ice (Painter and others, 2007). Furthermore, ferric oxide minerals have the capacity to absorb metals and thereby have relevance to human-health issues approached through our bioaccessibility methods.

A central contribution of this study is a demonstration of combined techniques to determine with high specificity the iron oxide minerals in atmospheric dust. Most importantly, we identified by multiple, independent methods the presence of goethite, possibly nanosized. The presence of hematite was detected using Mössbauer spectroscopy and magnetization measurements but was not convincingly supported by other methods.

There are too few samples from the NDRA to draw any inferences about relations among magnetic properties, iron mineralogy, and radiative properties. Nevertheless, the data for these samples contribute to data accumulated for atmospheric dust originating from source regions elsewhere in North America, Australia, as well as southern and northern Africa (Moskowitz and others, 2011; Reynolds and others, 2011). The values for reflectance and magnetic properties of the samples from the NDRA are very tightly grouped relative to the ranges of values obtained from the much larger, global dust suite.

In vitro bioaccessibility tests are becoming more commonly used in the United States, especially to examine contaminated, urban, and geogenic or naturally produced Earth materials. Controls on element mobility and bioaccessibility may include particle size, soil pH, and the presence and types of clays and (or) iron or manganese oxides. Mineral phase is an important control on lead and arsenic bioaccessibility (Ruby and others, 1996). In these experiments on the samples from the NDRA, solution pH was evaluated as the primary variable on element mobility because particle sizes are nearly the same for all samples and because of a lack of information on mineral forms. Extrapolation of the IVBA results to human health risk is difficult because many physiological factors control uptake of elements by the body. With the exception of lead (U.S. Environmental Protection Agency, 2008), little work has been done to evaluate bioaccessible concentrations for other elements or their application in determining relative bioavailability values in an environmental setting where exposures are generally low dose but chronic. Nonetheless, for some metals (arsenic, cadmium, copper, manganese, lead, and uranium), upwards of 50 percent of the total concentrations are soluble in the simulated body fluids, particularly in the SGF. Despite the uncertainties with factors that control the uptake of these metals by the body, the elevated solubilities of these metals may lead to associated health risks.

The methodology and data presented in this report not only complement ongoing studies but also prescribe techniques and provide information for future studies of the effects of dust within the NDRA and globally. The ability to characterize atmospheric dust in terms of iron phases, iron oxide mineralogy, radiative properties, and bioaccessibility is essential for understanding dust effects from local to global scales.

References Cited

Bradham, K.D., Scheckel, K.G., Nelson, C.M., Seales, P.E., Lee, G.E., Hughes, M.F., Miller, B.W., Yeow, Aaron, Gilmore, Thomas, Serda, S.M., Harper, Sharon, and Thomas, D.J., 2011, Relative bioavailability and bioaccessibility and speciation of arsenic in contaminated soils: Environmental Health Perspectives, v. 119, no. 11, p. 1629–1634. (Also available at http://dx.doi.org/10.1289/ehp.1003352.)

Brand, R.A., 1987, Improving the validity of hyperfine field distributions from metallic alloys—Part I—Unpolarized source: Nuclear Instruments and Methods in Physics Research, section B, v. 28, no. 3, p. 398–416.

Briggs, P.H., and Meier, A.L., 2002, The determination of forty-two elements in geological materials by inductively coupled plasma-mass spectrometry, chap. I *of* Taggart, J.E., Jr., ed., Analytical methods for chemical analysis of geologic and other materials: U.S. Geological Survey Open-File Report 02–223, p. I–1—I–14. (Also available at http://pubs.usgs.gov/of/2002/ofr-02-0223/OFR-02-0223.pdf.)

Clark, R.N., Swayze, G.A., Wise, R.A., Livo, K.E., Hoefen, T.M, Kokaly, R.F., and Sutley, S.J., 2007, USGS digital spectral library splib06a: U.S. Geological Survey Data Series 231, available at http://speclab.cr.usgs.gov/spectral.lib06/ds231/index.html.

Drexler, J.W., and Brattin, W.J., 2007, An in vitro procedure for estimation of lead relative bioavailability; with validation: Human and Ecological Risk Assessment, v. 13, p. 383–401. (Also available at http://www.tandfonline.com/doi/abs/10.1080/10807030701226350.)

Fabian, Karl, 2003, Some additional parameter to estimate domain state from isothermal magnetization measurements: Earth and Planetary Science Letters, v. 213, nos. 3–4, p. 337–345. (Also available at http://www.sciencedirect.com/science/article/pii/S0012821X03003297.)

Formenti, P., Schuetz, L., Balkanski, Y., Desboeufs, K., Ebert, M., Kandler, K., Petzold, A., Scheuvens, D., Weinbruch, S., and Zhang, D., 2010, Recent progress in understanding physical and chemical properties of mineral dust: Atmospheric Chemistry and Physics Discussions, v. 10, p. 31187–31251.

Gassó, Santiago, Grassian, V.H., and Miller, R.L., 2010, Interactions between mineral dust, climate, and ocean ecosystems: Elements, v. 6, no. 4, p. 247–252. (Also available at http://elements.geoscienceworld.org/content/6/4/247.abstract.)

Goossens, Dirk, 2012, A method for dry extracting large volumes of fine particulate matter from bulk soil samples: Air Quality Atmosphere and Health, v. 5, no. 4, p. 425–431. (Also available at http://rd.springer.com/article/10.1007/s11869-011-0142-7.)

Goossens, Dirk, and Buck, Brenda, 2009a, Dust dynamics in off-road vehicle trails—Measurements on 16 arid soil types, Nevada, USA: Journal of Environmental Management, v. 90, p. 3458–3469. (Also available at http://www.sciencedirect.com/science/article/pii/S0301479709001972.)

Goossens, Dirk, and Buck, Brenda, 2009b, Dust emission by off-road driving—Experiments on 17 arid soil types, Nevada, USA: Geomorphology, v. 107, nos. 3–4, p. 118–138. (Also available at http://www.sciencedirect.com/science/article/pii/S0169555X08005266.)

Goossens, Dirk, and Buck, Brenda, 2011a, Effects of wind erosion, off-road vehicular activity, atmospheric conditions and the proximity of a metropolitan area on PM10 characteristics in a recreational site: Atmospheric Environment, v. 45, no. 1, p. 94–107. (Also available at http://www.sciencedirect.com/science/article/pii/S1352231010008228.)

Goossens, Dirk, and Buck, Brenda, 2011b, Gross erosion, net erosion and gross deposition of dust by wind: field data from 17 desert surfaces: Earth Surface Processes and Landforms, v. 36, no. 5, p. 610–623. (Also available at http://onlinelibrary.wiley.com/doi/10.1002/esp.2080/abstract.)

Goossens, D., Buck, B., and McLaurin, B., 2012, Contributions to atmospheric dust production of natural and anthropogenic emissions in a recreational area designated for off-road vehicular activity (Nellis Dunes, Nevada, USA): Journal of Arid Environments, v. 78, p. 80–99. (Also available at http://www.sciencedirect.com/science/article/pii/S0140196311003168.)

Guyodo, Yohan, Mostrom, Alison, Penn, R.L., Banerjee, S.K., 2003, From nanodots to nanorods—Oriented aggregation and magnetic evolution of nanocrystalline goethite: Geophysical Research Letters, v. 30, 1512, 4 p. (Also available at http://www.agu.org/pubs/crossref/2003/2003GL017021.shtml.)

Herting, Gunilla, Wallinder, I.O., and Leygraf, Christofer, 2006, Factors that influence the release of metals from stainless steels exposed to physiological media: Corrosion Science, v. 48, no. 8 p. 2120–2132. (Also available at http://www.sciencedirect.com/science/article/pii/S0010938X05002465.)

Jackson, Mike, and Solheid, Peter, 2010, On the quantitative analysis and evaluation of magnetic hysteresis data: Geochemistry Geophysics Geosystems, v. 11, Q04Z15, 25 p. (Also available at http://www.agu.org/pubs/crossref/2010/2009GC002932.shtml.)

King, J.W., and Channel, J.E.T., 1991, Sedimentary magnetism, environmental magnetism, and magnetostratigraphy: Reviews of Geophysics, v. 29, supplement, p. 358–370.

Kokaly, R.F., 2011, PRISM—Processing routines in IDL for spectroscopic measurements (installation manual and user's guide, version 1.0): U.S. Geological Survey Open-File Report 2011–1155, 431 p., available at http://pubs.usgs.gov/of/2011/1155/.

Lamothe, P.J., Meier, A.L., and Wilson, S.A., 2002, The determination of forty-four elements in aqueous samples by inductively coupled plasma-mass spectrometry, chap. H *of* Taggart, J.E., Jr., ed., Analytical methods for chemical analysis of geologic and other materials: U.S. Geological Survey Open-File Report 02–223, p. H–1—H–14. (Also available at http://pubs.usgs.gov/of/2002/ofr-02-0223/OFR-02-0223.pdf.)

Lee, A., Lee, E.G., Lee, T., Kim, S.W., Slaven, J.E., and Harper, M., 2011, Size-selective sampling of particulates using a physiologic sampling pump: Journal of Environmental Monitoring, v. 13, no. 3, p. 527–535. (Also available at http://www.ncbi.nlm.nih.gov/pubmed/21234496.)

Liu, Qingsong, Yu, Yongjae, Torrent, José, Roberts, A.P., Pan, Yongxin, and Zhu, Rixiang, 2006, Characteristic low-temperature magnetic properties of aluminous goethite [α-(Fe, Al)OOH] explained: Journal of Geophysical Research, v. 111, B12S34, 12 p. (Also available at http://www.agu.org/pubs/crossref/2006/2006JB004560.shtml.)

McLaurin, B.A.T., Goossens, Dirk, and Buck, B.J., 2011a, Combining surface mapping and process data to assess, predict, and manage dust emissions from natural and disturbed land surfaces: Geosphere, v. 7, no. 1, February, p. 260–275. (Also available at http://geosphere.gsapubs.org/content/7/1/260.abstract.)

McLaurin, Brett, Goossens, Dirk, and Buck, Brenda, 2011b, Physical settings of the Nellis Dunes Recreation Area, chap. 2 of Goosens, Dirk, and Buck, B.J., eds., Assessment of dust emissions, chemistry, and mineralogy for management of natural and disturbed surfaces at Nellis Dunes recreation area, Nevada: Las Vegas, Nevada, University of Nevada Las Vegas, p. 13–39. (Also available at http://www.blm.gov/nv/st/en/fo/lvfo/blm_programs/more/nellis_dunes_dust.html.)

Morin, F.J., 1950, Magnetic susceptibility of α-Fe_2O_3 and α-Fe_2O_3 with added titanium: Physical Review, v. 78, no. 6, p. 819–820.

Morman, S.A., Plumlee, G.S., and Smith, D.B., 2009, Application of in vitro extraction studies to evaluate element bioaccessibility in soils from a transect across the United States and Canada: Applied Geochemistry, v. 24, no. 8, p. 1454–1463. (Also available at ftp://nrn1.nrcan.gc.ca/ess/geochem/files/miscel/env_health/applied_geochem_v24_issue8/p1454_1463.pdf.)

Moskowitz, B., Yauk, K., Till, J., Berquó, T., Banerjee, S.K., Reynolds, R.L., and Goldstein, H.L., 2011, Magnetic properties of iron oxide minerals in atmospheric dust and source sediments from western US: Eos, Transactions of the American Geophysical Union fall meeting supplement, abstract U11A–0002. (Also available at http://www.agu.org/meetings/fm11/waisfm11.html.)

Murad, Enver, and Johnston, J.H., 1987, Iron oxides and oxyhydroxides, *in* Long, G.J., ed., Mössbauer spectroscopy applied to inorganic chemistry: New York, Springer, v. 2, p. 507–582.

Painter, T.H., Barrett, A.P., Landry, C.C., Neff, J.C., Cassidy, M.P., Lawrence, C.R., McBride, K.E., and Farmer, G.L., 2007, Impact of disturbed desert soils on duration of mountain snow cover: Geophysical Research Letters, v. 34, L12502, 6 p. (Also available at http://www.agu.org/pubs/crossref/2007/2007GL030284.shtml.)

Reynolds, R.L., Goldstein, H.L., Moskowitz, B.M., Till, J.L., Flagg, C., Kokaly, R.F., Munson, S., Landry, C., Lawrence, C.R., Hiza, M.M., D'Odorico, P., and Painter, T.H., 2011, Iron oxide minerals in atmospheric dust and source sediments—Studies of types and properties to assess environmental effects: Eos, Transactions of the American Geophysical Union Fall Meeting Supplement Abstract U13B–01. (Also available at http://www.agu.org/meetings/fm11/waisfm11.html.)

Rochette, Pierre, Mathé, P.-E., Esteban, Lionel, Rakoto, Harison, Bouchez, J.-L., Liu, Qingsong, and Torrent, José, 2005, Non-saturation of the defect moment of goethite and fine-grained hematite up to 57 teslas: Geophysical Research Letters, v. 32, L22309, 4 p. (Also available at http://www.agu.org/pubs/crossref/2005/2005GL024196.shtml.)

Ruby, M.V., Davis, Andy, Schoof, Rosalind, Eberle, Steve, and Sellstone, C.M., 1996, Estimation of lead and arsenic bioavailability using a physiologically based extraction test: Environmental Science and Technology, v. 30, no. 2, p. 422–430. (Also available at http://pubs.acs.org/doi/abs/10.1021/es950057z.)

Smirnov, A.V., 2009, Grain size dependence of low-temperature remanent magnetization in natural and synthetic magnetite—Experimental study: Earth Planets Space, v. 61, no. 1, p. 119–124. (Also available at http://www.terrapub.co.jp/journals/EPS/pdf/2009/6101/61010119.pdf.)

Soukup, Deborah, Buck, Brenda, Goossens, Dirk, Ulery, April, McLaurin, B.T., Baron, Dirk, and Teng, Yuanxin, 2012, Arsenic concentrations in dust emissions from wind erosion and off-road vehicles in the Nellis Dunes recreational area, Nevada, USA: Aeolian Research, v. 5, August, p. 77–89. (Also available at http://www.sciencedirect.com/science/article/pii/S1875963711000851.)

Stefaniak, A.B., Guilmette, R.A., Day, G.A. Hoover, M.D., Breysse, P.N., and Scripsick, R.C., 2005, Characterization of phagolysosomal simulant fluid for study of beryllium aerosol particle dissolution: Toxicology in Vitro, v. 19, no. 1, p. 123–134. (Also available at http://www.sciencedirect.com/science/article/pii/S0887233304001250.)

Stefaniak, A.B., Day, G.A., Hoover, M.D., Breysse, P.N., and Scripsick, R.C., 2006, Differences in dissolution behavior in a phagolysosomal simulant fluid for single-constituent and multi-constituent materials associated with beryllium sensitization and chronic beryllium disease: Toxicology in Vitro, v. 20, no. 1, p. 82–95. (Also available at http://www.sciencedirect.com/science/article/pii/S0887233305001098.)

U.S. Environmental Protection Agency, 2008, Standard operating procedure for an in vitro bioaccessibility assay for lead in soil: U.S. Environmental Protection Agency EPA 9200.1–86. (Also available at http://www.epa.gov/superfund/bioavailability/pb_ivba_sop_final.pdf.)

Van Wijnen, J.H., Clausing, P., and Brunekreef, B., 1990, Estimated soil ingestion by children: Environmental Research, v. 51, no. 2, p. 147–162. (Also available at http://www.sciencedirect.com/science/article/pii/S0013935105800854#.)

Verwey, E.J., 1939, Electronic conduction of magnetite (Fe_3O_4) and its transition point at low temperatures: Nature, v. 144, no. 3642, p. 327–328. (Also available at http://www.nature.com/nature/journal/v144/n3642/pdf/144327b0.pdf.)

Publishing support provided by:
Denver Publishing Service Center

For more information concerning this publication, contact:
Center Director, USGS Geosciences and Environmental Change Science Center
Box 25046, Mail Stop 980
Denver, CO 80225
(303) 236-5344

Or visit the Geosciences and Environmental Change Science Center Web site at: *http://gec.cr.usgs.gov/*

(303) 236-1562

Or visit the Central Mineral and Environmental Resources Science Center Web site at: *http://minerals.cr.usgs.gov/*

USGS

Goldstein and others—**Iron Mineralogy and Bioaccessibility—Nellis Dunes Recreational Area, Nevada**—Scientific Investigations Report 2013–5054